Effect of annealing on nanoindentation slips in a bulk metallic glass

J. Patrick Coleman, Fanqiang Meng, Koichi Tsuchiya, James Beadsworth, Michael LeBlanc, Peter K. Liaw, Jonathan T. Uhl, Richard L. Weaver, and Karin A. Dahmen

Phys. Rev. B **96**, 134117 — Published 19 October 2017

DOI: 10.1103/PhysRevB.96.134117

The Effect of Annealing on Nanoindentation Slips in a Bulk Metallic Glass

J. Patrick Coleman*[1], Fanqiang Meng*[2], Koichi Tsuchiya[2, 3], James Beadsworth[1], Michael LeBlanc[1], Peter K. Liaw[4], Jonathan T. Uhl[5], Richard L. Weaver[1], and Karin A. Dahmen[1]

[1]Department of Physics and Institute for Condensed Matter Theory, University of Illinois at Urbana Champaign, 1110 West Green Street, Urbana, Illinois 61801, USA

[2]Research Center for Strategic Materials, National Institute for Materials Science, Sengen 1-2-1, Tsukuba, Ibaraki 305-0047, Japan

[3]Graduate School of Pure and Applied Sciences, University of Tsukuba, Tennoudai 1-1, Tsukuba, Ibaraki 305-8577, Japan

[4]Department of Materials Science and Engineering, The University of Tennessee, Knoxville, TN 37996, USA

[5] retired.

*First authors

We measure and analyze the statistics of nanoindentation pop-ins in a bulk metallic glass that has been annealed after being subjected to high pressure torsion. We argue that these pop-ins are avalanches of slip events. Larger slip avalanches are observed after annealing at higher temperatures. The slip avalanche size distribution shows scaling behavior and suggests the existence of a critical annealing temperature. Results are shown to be consistent with the predictions of a simple mean field theory. This implies that the statistics of slip avalanches in nanoindentation can be used to extract information about the structure, history, density and free volume of the material. The methods employed here are expected to be applicable to a wide range of materials.

I. INTRODUCTION

Bulk metallic glasses (BMGs) are amorphous alloys with superior strength compared to conventional crystalline metals [1]. But due to their tendency for sudden failure, BMGs are limited in their applications [1-20]. To improve the usefulness of BMGs, a better understanding of their deformation properties is sought. When a nanoindenter tip is pushed into a BMG sample under a slowly increasing load, the BMG exhibits pop-in events that come in a wide range of sizes. These pop-in events are correlated with the activation of shear bands [6]. It has been shown that slip events observed in BMGs during uniaxial compression progress via avalanches of elastically coupled weak spots [7, 8]. We extend that analysis here to the pop-in events observed in nanoindentation of BMGs, suggesting that each pop-in corresponds to an avalanche of slip events.

Previous studies [21] have revealed that high pressure torsion (HPT) deformation leads to a significant decrease in nanoindentation hardness and elastic modulus, as well as a change in the deformation mode from shear band formation to homogeneous deformation without shear band formation. Relaxation by subsequent annealing can partially reverse some of the effects of the prior HPT deformation and increase the extent of shear banding [22]. As the annealing temperature is increased, the fictive temperature decreases [23] and the free volume decreases [22]. There have also been experiments to show that severe plastic deformation (SPD) can affect the presence of serrated flows in BMGs [24].

We observe in this paper that the statistics of slip avalanches seen during nanoindentation of a BMG that has undergone HPT depend on the temperature at which the BMG was annealed. Lower annealing temperatures lead to smaller slip avalanches while higher annealing temperatures lead to larger slip avalanches. We extract the statistics of these events from many indentations and then compare the results to expectations based on an approach to a critical annealing temperature [25]. We hypothesize that there are two different types of slip avalanches occurring in nanoindentation experiments, as was found of slips events in uniaxial compression experiments [7, 8]. We show that the smaller slip events are scale invariant, as was found for uniaxial compression of BMGs [7, 8]. We find a scaling collapse of the complementary cumulative distribution functions (CCDFs) of the slip avalanche sizes is possible with data from three different annealing temperatures. This suggests the presence of a critical annealing temperature where power law distributions of slip avalanches are observed.

II. EXPERIMENT

Master alloy ingots of $Zr_{50}Cu_{40}Al_{10}$ in atomic percent were prepared by arc-melting pure Zr, Cu, and Al elements in an argon atmosphere. The mother ingots of the alloy were completely remelted at least three times and then cast into a cylindrical rod with diameter 10mm by the tilt-casting method in an arc furnace. X-ray analysis shows that the as-cast

sample is fully amorphous. The disk for this experiment was sliced from the as-cast rod with an original thickness of 0.85 mm. The disk was subjected to high-pressure torsion (HPT) under a pressure of 5 GPa at room temperature for 50 revolutions which brought its thickness down to near 0.8mm. X-ray diffraction (XRD) and high-resolution transmission electron microscopy (HRTEM) results indicate the amorphous nature and absence of crystallization after 50 revolutions. The geometry of the HPT experiment is shown in Fig. 2, along with XRD graphs.

Annealing treatments were performed using a Perkin Elmer Diamond Differential Scanning Calorimeter (DSC). The specimen was heated to 150°C at a heating rate of 0.667°C/s followed by a subsequent cooling to room temperature at a rate of 1.667°C/s; there was no holding period at the annealing temperature. The annealed sample was then mirror-like polished using a 0.06 μm SiO_2 colloidal suspension. Forty-nine nanoindentations were carried out. The sample was then annealed to 200°C at the same heating rate (0.667°C/s) and the same cooling rate (1.667°C/s). A few micrometers were removed with grinding paper to remove any trace of the previous indentations. The sample was then re-polished and subjected to forty-nine more nanoindentations. The sample was thus repeatedly annealed, ground, polished, and indented in this way for annealing temperatures 250°C, 300°C, 350°C, and 400°C. A schematic illustration of the annealing treatment is shown in Fig. 4.

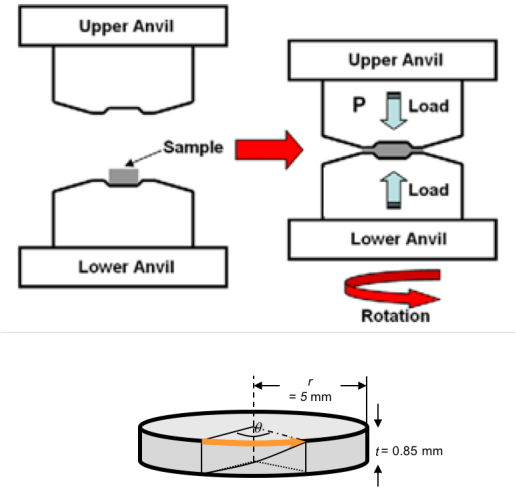

Fig. 1: Geometry of high-pressure torsion experiment. A disk sample (10mm diameter and 0.85mm thickness) is placed between two cylindrical anvils. A compressive load (typically 5GPa) is applied and the lower anvil is rotated at a constant speed.

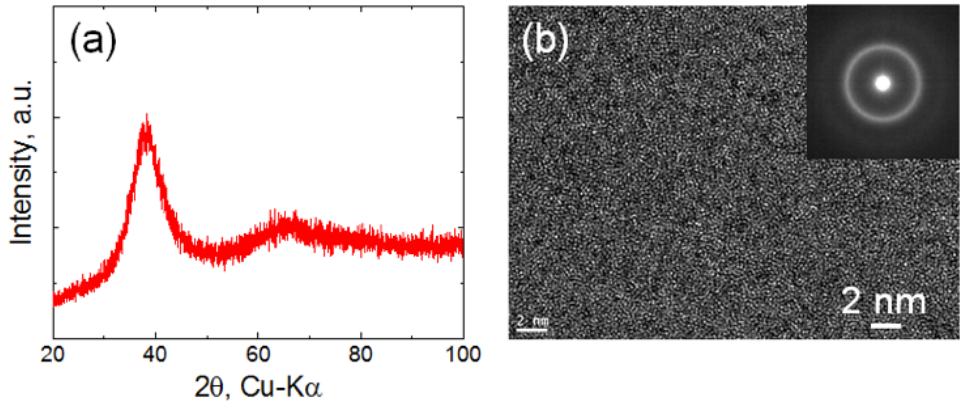

Fig. 2: (a) X-ray diffraction pattern and (b) high-resolution transmission electron microscopy image with corresponding selected area diffraction pattern from $Zr_{50}Cu_{40}Al_{10}$ BMG deformed by HPT with 50 revolutions.

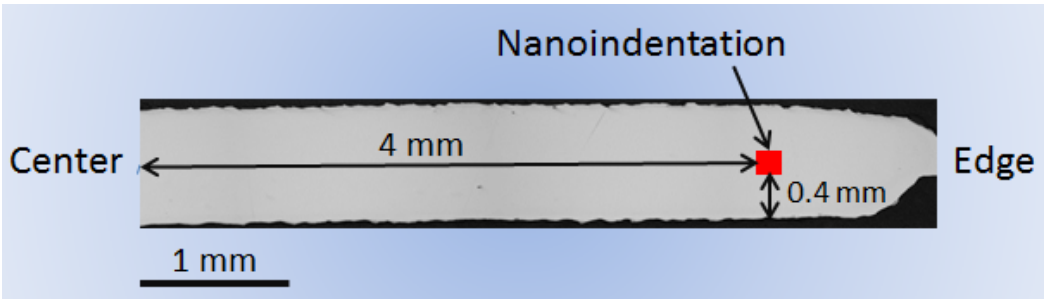

Fig. 3: Optical microscopy image of the cross-section of the sample deformed with 50 revolutions. The red square indicates the 36 x 36 μm² region for the nanoindentation tests.

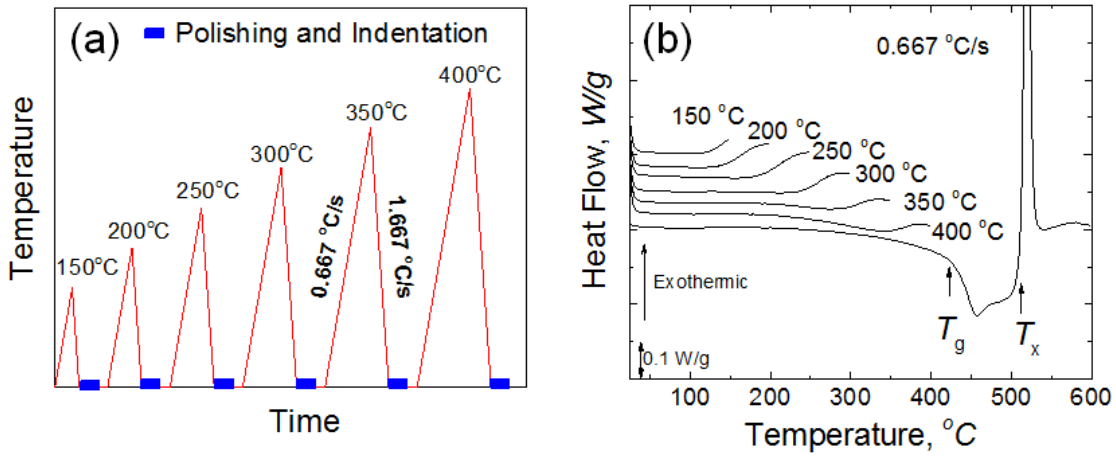

Fig. 4: (a) Schematic illustration of annealing treatments and polishing and nanoindentation tests; (b) DSC heating curves for each heating cycle. There is an exothermic peak corresponding to structural relaxation when the peak temperatures range

from 150°C to 400°C, and the onset temperature of relaxation rises after each heating run. The increase of onset temperature in each curve reveals that the amount of free volume is dependent on the annealing temperature. The sample was heated up to 600°C to see the glass transition and crystallization peaks.

Nanoindentation was carried out with a Hysitron Triboindenter TI950. All nanoindentations were done on the same specimen, which was a quarter-disk obtained by cutting the as-deformed disk along perpendicular planes, each of which contained the cylindrical axis. The indentation procedure consisted of a loading segment of 20 s at a rate of 250 μN/s, followed by a holding segment of 20 s at the maximum load of 5000 μN, and then an unloading segment of 20 s. The position of the nanoindentations is 4mm from what was the center of the disk before quartering. The nanoindentations took place at 49 points, forming a 7 x 7 grid with the distance between adjacent points being 6 μm. The whole grid formed an area of 36 x 36 μm^2. An image of the sample is shown in Fig. 3 with the position of the nanoindentation tests marked.

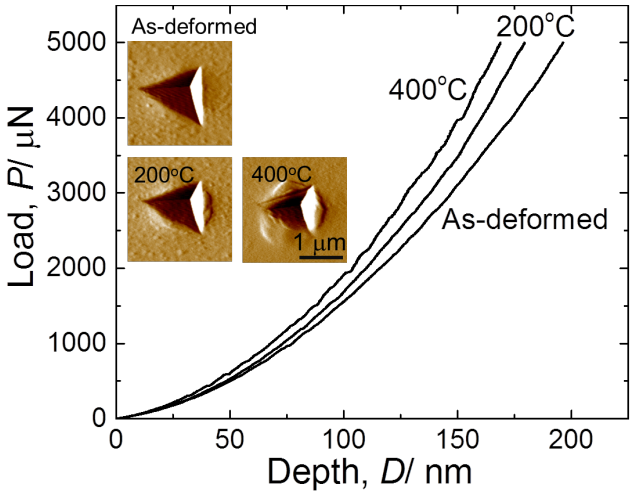

Fig. 5. Typical load-depth curves of the as-deformed $Zr_{50}Cu_{40}Al_{10}$ BMG, and after annealing at 200°C and 400°C. The inset shows scanning probe microscope images of indents.

III. DATA ANALYSIS

We construct CCDFs from the nanoindentation data to show the size of slip avalanches for each annealing temperature. The CCDF, *C(S)*, of slip size, *S*, gives the fraction of slip avalanches that are larger than size *S*. We devised two methods for calculating the size of a slip avalanche. The first method defines a signal s_1(t):

$$s_1(t) = \frac{\Delta\sigma(t)}{\Delta t} \cdot D(t)^w \#[1]$$

$$\sigma(t) = \frac{F(t)}{D(t)^2} \#[2]$$

where $\sigma(t)$ is proportional to the stress under the indenter tip, $F(t)$ is the force applied to the indenter tip, $D(t)$ is the displacement of the indenter tip, Δt is the reciprocal of the sampling frequency (Δt =0.0500 s), and w is an exponent chosen so that $s_1(t)$ would have roughly constant average peak amplitudes throughout the 20 seconds of increasing load (w = 1.4 for our analysis). Since slip avalanches produce a drop in the stress on the indenter tip, slip avalanches appear as sharp negative spikes in $s_1(t)$. After using a small threshold to filter out the spikes due to noise, the remaining spikes are counted. The slip avalanche begins when $s_1(t)$ drops below the threshold, and it ends when the signal crosses back above the threshold. Motivated by a mean field model [25], we define the size of the slip avalanche, S, as the difference in stress $\sigma(t)$ from the start of the slip avalanche to its end multiplied by $D(t_i)^{1.4}$ where t_i is the start time of the slip avalanche. Thus the size of the slip avalanche is approximately equal to the area under the spike in $s_1(t)$. Fig. 8 shows $C(S)$ for six different annealing temperatures using the above definition of slip avalanche size. The minimum slip avalanche size shown in the plots of Fig. 7 is the smallest size for which power-law behavior is observed. Figures showing the entire CCDF for each temperature including the smallest observed slip avalanche sizes are included in the appendix.

An alternate definition of slip avalanche size uses only the displacement of the indenter tip. In nanoindentation, the displacement of the indenter tip is roughly proportional to the square root of the applied load [26], as is apparent in Fig. 5. This trend produces an overall feature in the time derivative proportional to $\frac{1}{\sqrt{t}}$. To better identify slip avalanches, the reciprocal square root trend is subtracted from the discretely differenced displacement signal:

$$s_2(t) = \frac{\Delta D(t)}{\Delta t} - \left(a + \frac{b}{\sqrt{t}}\right). \#[3]$$

The coefficients a and b are those of a least-squares fit to $\frac{\Delta D(t)}{\Delta t}$. Large positive spikes in $s_2(t)$ correspond to slip avalanches. Again we used a small threshold to filter out spikes due to noise. Slip avalanches were counted in a similar manner as in the first method: when $s_2(t)$ exceeds the threshold the slip avalanche begins, and when it drops below the threshold the slip avalanche ends. The size of the slip avalanche is the total change in the displacement of the indenter tip during the duration of the slip. In the appendix, these two methods of defining slip avalanche size are compared, and it is shown that they give similar results.

IV. MODEL PREDICTIONS

In order to model the experimental results, we use a simple mean field model [25] that was previously shown to correctly predict the slip statistics and slip dynamics of bulk metallic glasses under slow compression [7, 27]. The model assumes that BMGs have weak spots

that slip when the local stress exceeds a random failure stress. The weak spots are elastically coupled and therefore a slipping weak spot can trigger other weak spots to also slip in a slip avalanche. In BMGs the slips occur generally along shear bands, thereby ensuring positive stress transfer between the weak spots that participate in the slip avalanches [28]. Our model [25] takes this positive stress transfer into account, in contrast to other models like [29, 30] that focus on other systems without permanent shear bands. Our model [25] also takes into account that BMGs weaken inside the shear bands, due to dilation. This weakening leads to 2 types of avalanches ("small" and "large" ones) which have different statistics and different dynamics. These 2 types of avalanches have also been found in experiments [7, 27]. Because of its simplicity and because of the strong agreement of the model predictions [25] with experiments on BMGs [7, 27], this model is a convenient starting point for a first analysis of the experiments in these materials.

The mean field theory model [25] predicts that *C(S)*, for scaling slip avalanches, should follow a power law multiplied by an exponentially decaying cut-off function. The cut-off function depends on experimentally tunable parameters; here we examine annealing temperature as the tunable parameter, and we extend this model to the geometry of nanoindentation.

For homogeneous applied stress F, and small weakening, the probability distribution function (PDF) of slip sizes S is predicted by the model to scale approximately as

$$D(S,F) \sim S^{-\tau} \cdot G\left(S \cdot (F_C - F)^2, Sv^{\theta}\right), \#[4]$$

as derived in [25, 31]. Here τ and θ are scaling exponents, F_C is a critical stress, v is a measure of the free volume in the material, which depends on the annealing temperature T, and G is a scaling function. To first approximation, for annealing temperatures near an appropriate critical annealing temperature T_C, we can write $v \sim (T_C - T)$ and derive a scaling relation for *D(S,F)* as a function of annealing temperature.

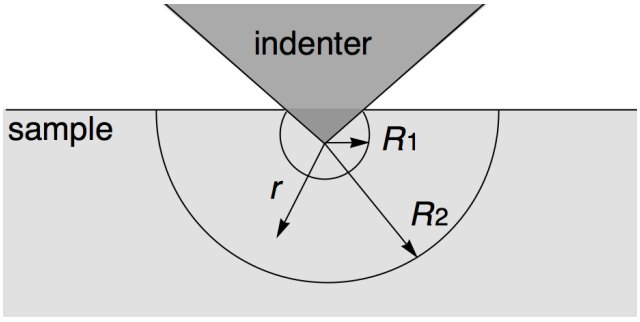

Fig. 6. Illustration of interaction between the indenter tip and the surface of the sample. The region immediately surrounding the indenter tip is the hydrostatic core, the region between R_1 and R_2 is the plastic region, and beyond R_2 is the elastic region [26]. The slip avalanches are expected to occur in the plastic region.

For nanoindentation experiments there are three regions in the sample: the hydrostatic core, the plastic region, and the elastic region as shown in Fig. 6 [26]. We expect slips to occur in the plastic region. We approximate the stress distribution in the plastic region to decay linearly to first order with the distance *r* from the indenter head, $F = F_C\left(1 - \frac{r-R_1}{R}\right)$ where R_1 is the radius at which the plastic region begins and R is simply a constant describing how quickly the stress decays. Inserting this form into Equation 4 and integrating over the plastic region in the half-space gives

$$D(S,T) \sim S^{-\tau} \int_{R_1}^{R_2} G\left(S \cdot \left(\frac{F_C \cdot (r - R_1)}{R}\right)^2, S \cdot (T_C - T)^\theta\right) 2\pi r^2 dr \#[5]$$

where R_2 is the radius at which the plastic region ends. If we make the change of variables $x = r\text{-}R_1$, then we have

$$D(S,T) \sim S^{-\tau} \int_0^{R_2 - R_1} G\left(S \cdot \left(\frac{F_C \cdot x}{R}\right)^2, S \cdot (T_C - T)^\theta\right) 2\pi (x + R_1)^2 dx. \#[6]$$

Since we expect *G* to become negligibly small for *x* values near the upper limit of the integral, we can let the upper limit go to infinity. Then we may make the substitution $u = S \cdot \left(\frac{Fc \cdot x}{R}\right)^2$ and obtain

$$D(S,T) \sim S^{-\tau-\frac{1}{2}} \int_0^\infty G\left(u, S \cdot (T_C - T)^\theta\right) \frac{\pi R}{F_C} \left(\left(\frac{R}{F_C}\right)^2 u S^{-1} + \frac{2RR_1}{F_C}\sqrt{u} S^{-\frac{1}{2}} + {R_1}^2\right) \frac{du}{\sqrt{u}} \#[7]$$

The integral can be broken up into the sum of three integrals, each of which, after pulling out all factors of *S*, can be rewritten in terms of a scaling function. This leaves us with a scaling relation for the PDF:

$$D(S,T) \sim S^{-\tau-\frac{3}{2}} \cdot f_1\left(S \cdot (T_C - T)^\theta\right) + S^{-\tau-1} \cdot f_2\left(S \cdot (T_C - T)^\theta\right)$$

$$+ S^{-\tau-\frac{1}{2}} \cdot f_3\left(S \cdot (T_C - T)^\theta\right) \#[8]$$

where the functions $f_i(x)$ are scaling functions. For small slip avalanche sizes we would expect the first term that goes as $S^{-\tau-\frac{3}{2}}$ to dominate. Exponential cut-offs are contained in the scaling functions $f_i(x)$, thus the maximum slip size $S_{\max}$ is related to annealing temperature $S_{\max} \sim (T_C - T)^{-\theta}$.

The CCDF, *C(S,T)*, is useful in systems with low numbers of slips. It may be calculated from D(S,T):

$$C(S,T) = \int_{-\infty}^{S} D(S',T)dS' \,.\#[9]$$

Combining Equations 8 and 9, and taking just one term from the resulting CCDF we have

$$C_i(S,T) \sim \int_{-\infty}^{S} S'^{p_i} \cdot f_i\big(S' \cdot (T_C - T)^{\theta}\big)dS' \,\#[10]$$

where p_i is the power of S in the *i-th* term. Making the substitution $w = S'(T_C - T)^{\theta}$ gives

$$C_i(S,T) \sim \int_{-\infty}^{S(T_C-T)^{\theta}} \frac{w^p}{(T_C - T)^{p\theta}} \cdot f_i(w) \frac{dw}{(T_C - T)^{\theta}} \,\#[11]$$

The factors of $(T_C - T)^{\theta}$ can be taken out of the integral to give

$$C_i(S,T) \sim (T_C - T)^{(-p-1)\theta} \int_{-\infty}^{S(T_C-T)^{\theta}} w^p f_i(w)dw \,.\#[12]$$

We can now define a universal scaling function

$$g_i\big(S(T_C - T)^{\theta}\big) = \big(S(T_C - T)^{\theta}\big)^{(-p-1)} \int_{-\infty}^{S(T_C-T)^{\theta}} w^p f_i(w)dw \,\#[13]$$

which gives us

$$C_i(S,T) \sim S^{p+1} \cdot g_i\big(S \cdot (T_C - T)^{\theta}\big). \#[14]$$

Summing all three terms gives us the scaling form of the CCDF:

$$C(S,T) \sim S^{-\tau-\frac{1}{2}} \cdot g_1\big(S \cdot (T_C - T)^{\theta}\big) + S^{-\tau} \cdot g_2\big(S \cdot (T_C - T)^{\theta}\big)$$

$$+S^{-\tau+\frac{1}{2}} \cdot g_3\big(S \cdot (T_C - T)^{\theta}\big). \#[15]$$

For small slip avalanches the first term dominates the distribution, as is confirmed by the data. That term is then used in Fig. 9 to collapse *C(S)* for three values of annealing temperature.

V. RESULTS

The size of slip avalanches is found to increase as the annealing temperature increases. This can be seen from the CCDFs shown in Fig. 7. BMGs exhibit two types of slip avalanches: smaller, “scaling” slip avalanches that are power-law distributed and larger, “spanning” slip

avalanches that span a macroscopic fraction of the indented region [7, 25,27]. To show that the smaller slip avalanches follow the predicted scaling form, we remove the spanning slip avalanches from the CCDFs of three annealing temperatures and perform a scaling collapse. The data for annealing temperatures T = 200°C, T = 250°C, and T = 300°C were chosen because they have smaller slip avalanches than the higher annealing temperatures, and therefore their power-law scaling regions are less likely to be distorted by finite size effects. The spanning slip avalanches are known to have different dynamics [7, 8, 25, 27], so we remove them by choosing a maximum size cut-off for each annealing temperature based on the dynamics of the slip avalanches seen in Fig. 8.

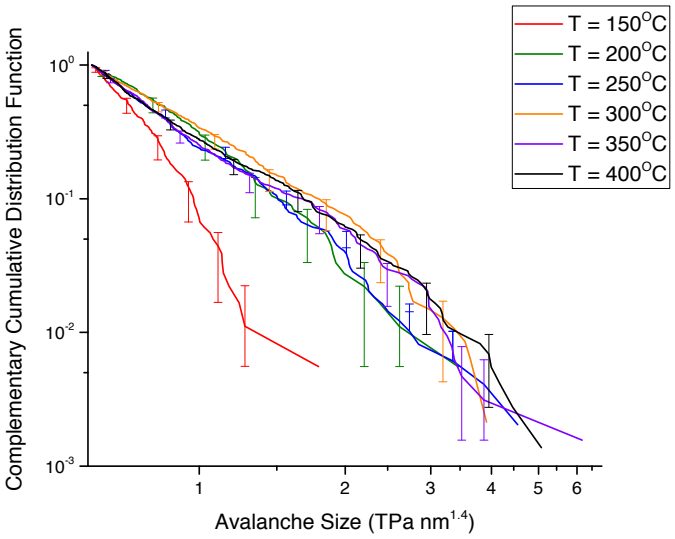

Fig. 7. Complementary cumulative distribution functions (CCDFs) for the slip avalanche sizes observed in all the trials using the first method of analysis, plotted for six annealing temperatures. Forty-nine trials were analyzed for each annealing temperature on a sample of $Zr_{50}Cu_{40}Al_{10}$. The avalanche size is defined in the text. The CCDFs show that on average the avalanche sizes tend to increase for increasing annealing temperature.

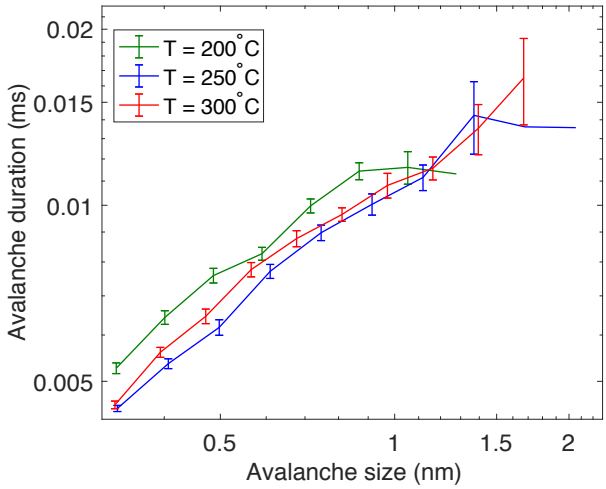

Fig. 8. Average value of slip avalanche durations as defined by the second method of analysis, binned by size. The flattening out observed for annealing temperatures T = 200°C and T = 250°C indicates a change in slip avalanche dynamics. The mean field predictions from [7, 8, 25] suggest that the slip avalanches in the flat regions are spanning slip avalanches rather than scaling slip avalanches. Thus we choose the size at which the curves flatten as the maximum slip size for those annealing temperatures. Consistent with the model predictions, we only obtained a scaling collapse of the CCDFs for slip avalanches smaller than those maximum sizes.

We collapse the CCDFs of the scaling slip avalanches using the first term from the scaling form from Equation 15:

$$C(S,T) \sim S^{-\tau-\frac{1}{2}} \cdot g_1\left(S \cdot (T_C - T)^{\theta}\right). \#[16]$$

The mean field theory values $\tau = \frac{3}{2}$ and $\theta = 2$ of the scaling exponents are used in the collapse in Fig. 9. The critical temperature T_C was estimated from the collapse to have a value T_C = 500°C (with a large error bar due to the statistical uncertainties of the data: the limits for τ are 1.3 to 1.7, while it appears that θ and T_c can vary together over a large range, from θ = 1.1, Tc=388°C to at least as high as θ = 6, Tc=1028°C). This wide error range for θ is not surprising as θ depends on the upper tail of the distribution that are given by the bigger of the scaling avalanches. Naturally there are not many of those bigger avalanches observed, so the statistical fluctuations in the tails of the distributions are large. Also the other terms in *C(S)* from Equation 12 can affect the upper tail of the distribution.

More experimental data with many more slip avalanches will enable us to narrow down the error bars on the critical exponents and the critical temperature in the future. It is remarkable however that the framework of the simple mean field model is consistent with the experimental data. Note that, since the crystallization temperature is 503°C, the highest possible values for T_C mentioned above are unphysical, which constrains the physically

possible range for θ to about $1.1 \leq \theta \leq 2$. The collapse shows that the data is consistent with the prediction of an underlying non-equilibrium critical point at a critical amount of free volume in the material that can be approached by increasing the annealing temperature. Using scaling collapses to test for the approach to a non-equilibrium critical point with associated universal power law scaling behavior has proven useful in many non-equilibrium systems with avalanches. The method and its applications to other avalanching systems is reviewed in more detail for example in [32].

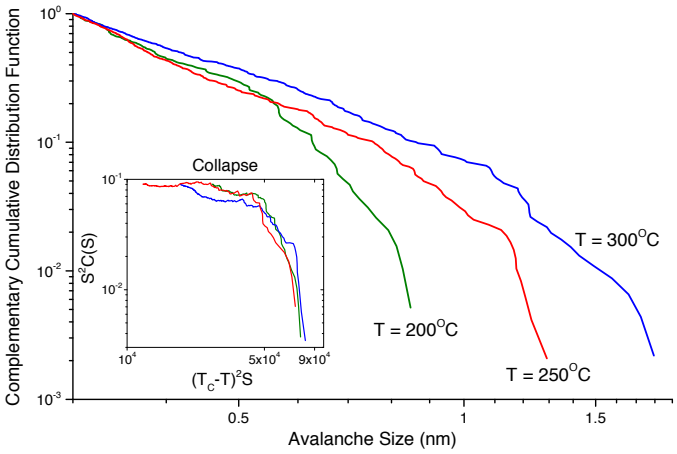

Fig. 9. CCDFs for slip avalanche sizes after removing the largest slip avalanches. The inset shows a scaling collapse of the CCDFs. The collapse variables τ and θ are set to their mean field theory values, which are $\tau = \frac{3}{2}$ and $\theta = 2$. The critical temperature was varied until the best collapse was found, which is at T_C = 500°C. The glass transition temperature for this sample of $Zr_{50}Cu_{40}Al_{10}$ is 424°C, which is lower but means that a critical temperature of 500°C is not unreasonable. As in Fig. 8, these are slip avalanches as defined by the second method of analysis.

VI. CONCLUSION

In summary, it is shown that annealing a sample of $Zr_{50}Cu_{40}Al_{10}$ BMG after HPT leads to larger slip avalanches being observed in nanoindentation as the annealing temperature rises. Two methods of detecting and analyzing slip avalanches from nanoindentation experiments have been suggested. These methods can be applied to the study of different materials in which plastic deformation progresses with slip avalanches. The methods employed here can be used to classify and distinguish different types of slip avalanches in nanoindentation experiments on a wide range of materials.

A simple mean field theory model, which was successful in describing the propagation of slip avalanches during uniaxial deformation of BMGs, has been adapted to the case of nanoindentation and has been shown to be consistent with experiment. The likely

existence of a critical point in annealing temperature for BMGs that have undergone HPT has been shown.

Acknowledgements:

We thank Wendelin Wright and Will McFaul for helpful discussions. We acknowledge support from the US National Science Foundation (NSF) through grants CBET 1336634 (KD), DMS 1069224 (KD & JPC), and DMR 1611180 (PKL). We also thank DOE for the support through project, DE-FE-0011194, with the project managers, Drs. Markovich and Mullen (KD & PKL).

APPENDIX: COMPARING THE ANALYSIS METHODS

Figs. 10 and 11 show complementary cumulative distribution functions (CCDFs) of slip avalanche sizes for annealing temperatures T= 150°C, 200°C, 250°C, 300°C, 350°C, and 400°C. Each plot was made with data from the same experiments, but the methods used to detect and analyze slip avalanches are different; the two methods are described in the paper. Fig. 10 is identical to Fig. 6 in the paper. It is shown here for comparison to Fig. 11. The data is taken from 294 experimental trials, 49 trials for each of the six annealing temperatures.

We will refer to the analysis method used to produce Fig. 10 as the first method. The data was analyzed as follows: For each trial the load (in microNewtons) and the total displacement of the indenter tip (in nanometers) are measured as a function of time. By dividing the load by the square of the total displacement we construct a quantity that is expected to be roughly proportional to the applied stress. A sudden drop in stress marks a slip avalanche. As the indenter tip moves further into the sample, though, the average stress decreases and the magnitude of the stress-drops decrease as well. To detect slip avalanches, we mark the points where the time derivative of the stress drops below a certain (noise-) threshold. But, since the magnitude of the fluctuations in the stress decreases as the indenter tip displacement grows, we rescale the time derivative of the stress by a factor of the indenter tip's displacement raised to the power of 1.4. That exponent was chosen because it appears to result in a steady signal when multiplied by the time derivative of the stress. The size of the slip avalanche is determined in this analysis method by calculating the magnitude of the stress-drop (that is, the difference between the initial stress and the final stress) and rescaling that by the total displacement at the time of the start of the avalanche raised to the power of 1.4. The slip avalanches are detected by setting a negative threshold value for the rescaled stress derivative. Any time the rescaled stress derivative signal drops below the threshold, the beginning of a slip avalanche is marked, and when the signal ceases to be below the threshold, the end of the slip avalanche is marked. The threshold value used in the CCDFs shown is the average value of the time derivative of the stress minus 1.7 times its standard deviation. In order to filter out tiny slip

avalanche signals, a minimum size is defined and all slip avalanches with sizes below the minimum are discarded. The minimum slip avalanche size used in this method is 600 GPa $nm^{1.4}$ because that's roughly the smallest size where power-law behavior is observed. Fig. 14 shows the CCDFs before the removal of slip avalanches below the minimum size.

In the second method of analysis, instead of looking for stress-drops in the stress signal, we look for sudden slips in the displacement signal itself. An avalanche is seen in the displacement signal by a sudden jump in displacement. If we look at the time derivative of the displacement signal, this is seen to be a positive spike. But the overall displacement signal increases roughly with the square root of the load, and since the load is increased linearly in time, it thus increases with the square root of the time. Thus the time derivative is roughly proportional to the reciprocal of the square root of time. In our method we fit a function $a + \frac{b}{\sqrt{t}}$ to the time derivative of the displacement using a least squares method and then subtract that fitted function from the derivative signal. Typical values of a are around -7 and typical values of b are around 50. What remains after the subtraction is the time derivative of the fluctuations about the square root trend. This signal is then analyzed by identifying spikes in a similar way as was done in the first method. A threshold is defined in a similar manner as in the previous method: the threshold is equal to the mean value plus 1.7 times the standard deviation of the signal after subtracting the fit. A minimum size for an avalanche is defined where the power law behavior begins in the CCDF and all avalanches smaller than it are ignored. The minimum size used for this method was 0.3nm. Figs. 14 and 15 show the CCDFs before the avalanches below the minimum size are removed.

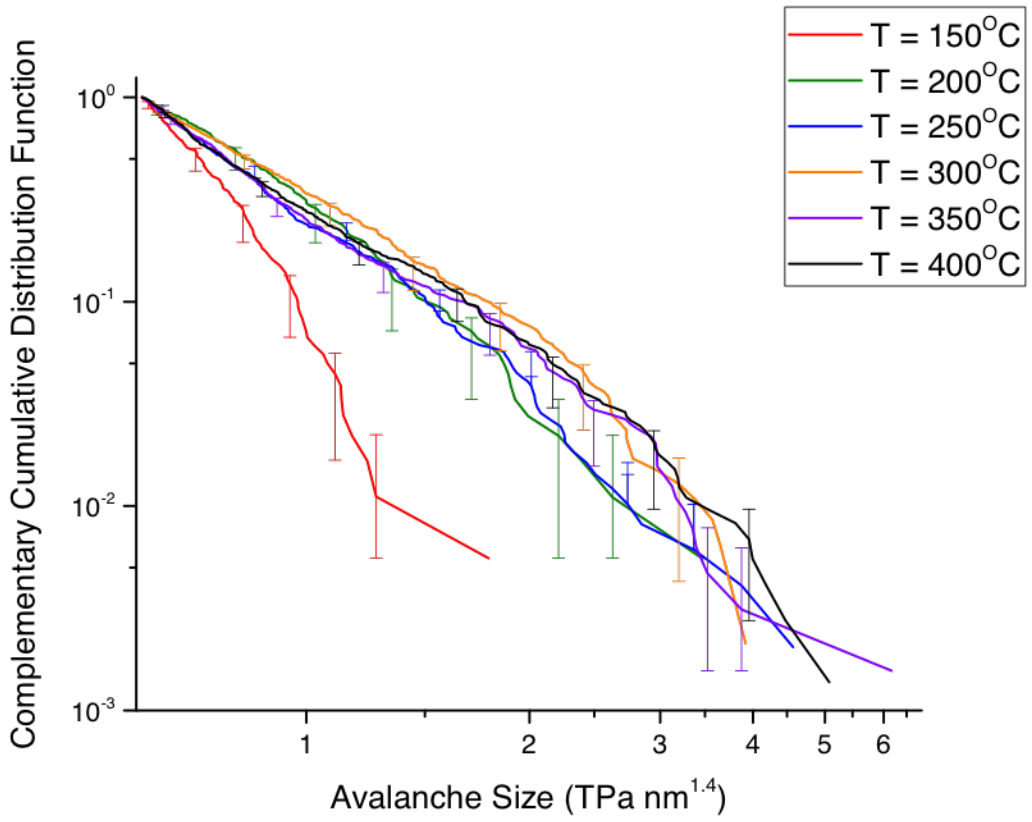

Fig. 10: Complementary cumulative distribution functions (CCDFs) of slip avalanche sizes using first method. Each of the CCDFs incorporates data from 49 experimental trials. The data from a single nanoindentation run consists of the load on the indenter head as a function of time and the total displacement of the indenter head as a function of time. Both of these quantities were sampled at a rate of 200Hz. In the analysis method used for this figure the load signal is divided by the square of the displacement signal in order to give a signal that is approximately proportional to the applied stress as a function of time. A sudden drop in stress, and thus a negative spike in its time derivative, signals a slip avalanche. But the variations in the time derivative of the stress were much larger for early times and much smaller for later times, so in order to find a signal that was roughly constant over the time of interest, the discretely differenced stress as a function of time was multiplied by the total displacement of the nanoindenter raised to the power of 1.4. When this signal dropped below the small negative threshold the start of the avalanche was marked, and when the signal came back above the threshold the end of the avalanche was marked. The size of the avalanche is defined as the change in stress from the beginning to the end of the avalanche multiplied by the total displacement at the beginning of the avalanche raised to the power of 1.4.

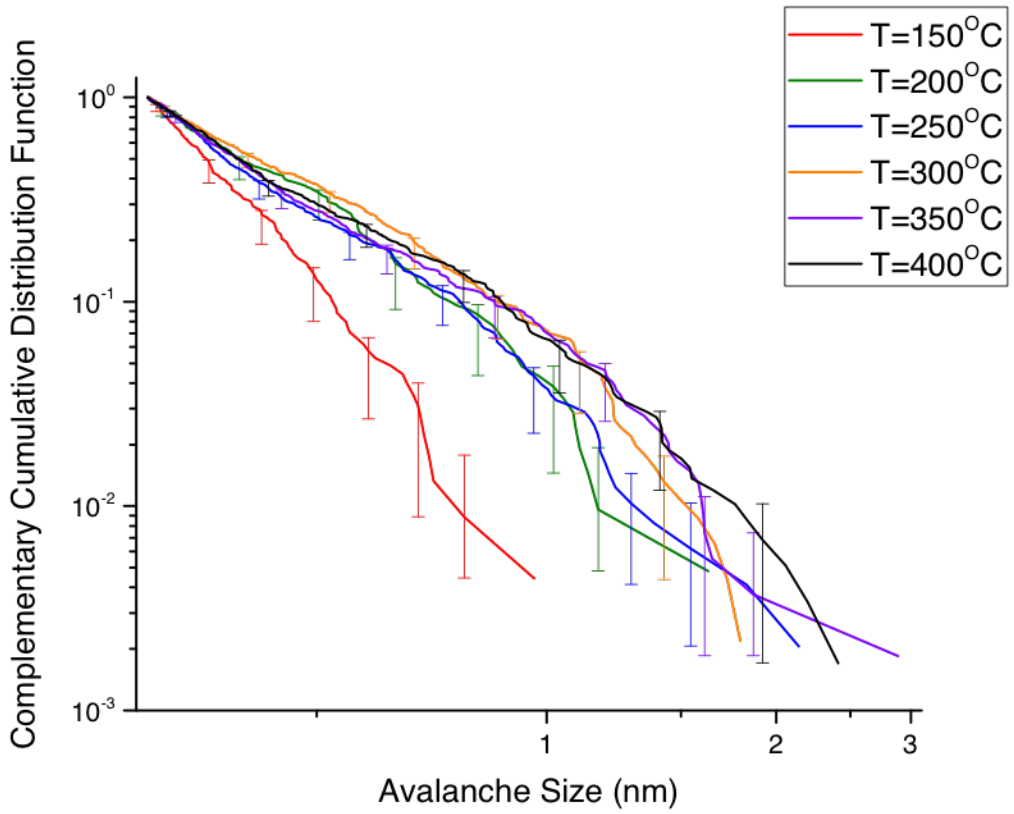

Fig. 11: CCDFs of slip avalanche sizes using the second method. This figure shows CCDFs of avalanche slip sizes taken from the same data as Fig. 13. But in the method of analysis used for this figure the displacement signal is discretely differenced to get a signal showing the derivative of the displacement with respect to time. A sudden rise in the displacement signals a slip avalanche, so positive spikes in the time derivative of the displacement should signal a slip avalanche. But the displacement signal has an overall trend that scales roughly like the square root of the time, thus the derivative has a trend that scales like the reciprocal of the square root. So a least-squares fit was done for the derivative signal and the resulting fit was subtracted off, leaving only the fluctuations in the derivative signal about the local mean. When this signal went above the small positive threshold the start of the avalanche was marked, and when the signal came back below the threshold the end of the avalanche was marked. The size of the avalanche is defined as the change in displacement from the beginning to the end of the avalanche.

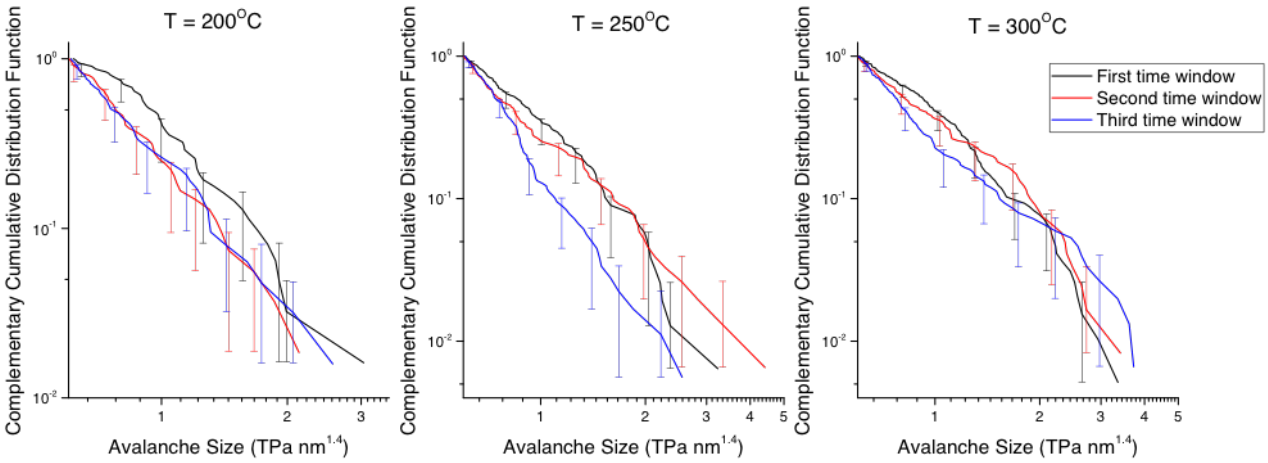

Fig. 12: CCDFs of slip avalanche sizes in TPa $nm^{1.4}$ created using the first analysis method for annealing temperatures T=200°C, T=250°C, and T=300°C. Each plot contains slip avalanches from a specific part of the trial: beginning, middle, or end. The slip avalanches were measured in the loading segment of the indentation, which was 20 seconds long. The windows divide the loading segment into thirds, so the CCDF for the first time window shows only those slip avalanches that occurred during the first third of the loading segment of a trial. Likewise the second time window shows those slip avalanches that occurred during the middle third, and the third time window shows those slip avalanches that occurred during the final third. These plots indicate that the slip avalanche sizes aren't strongly correlated with what time during the loading segment at which they occur.

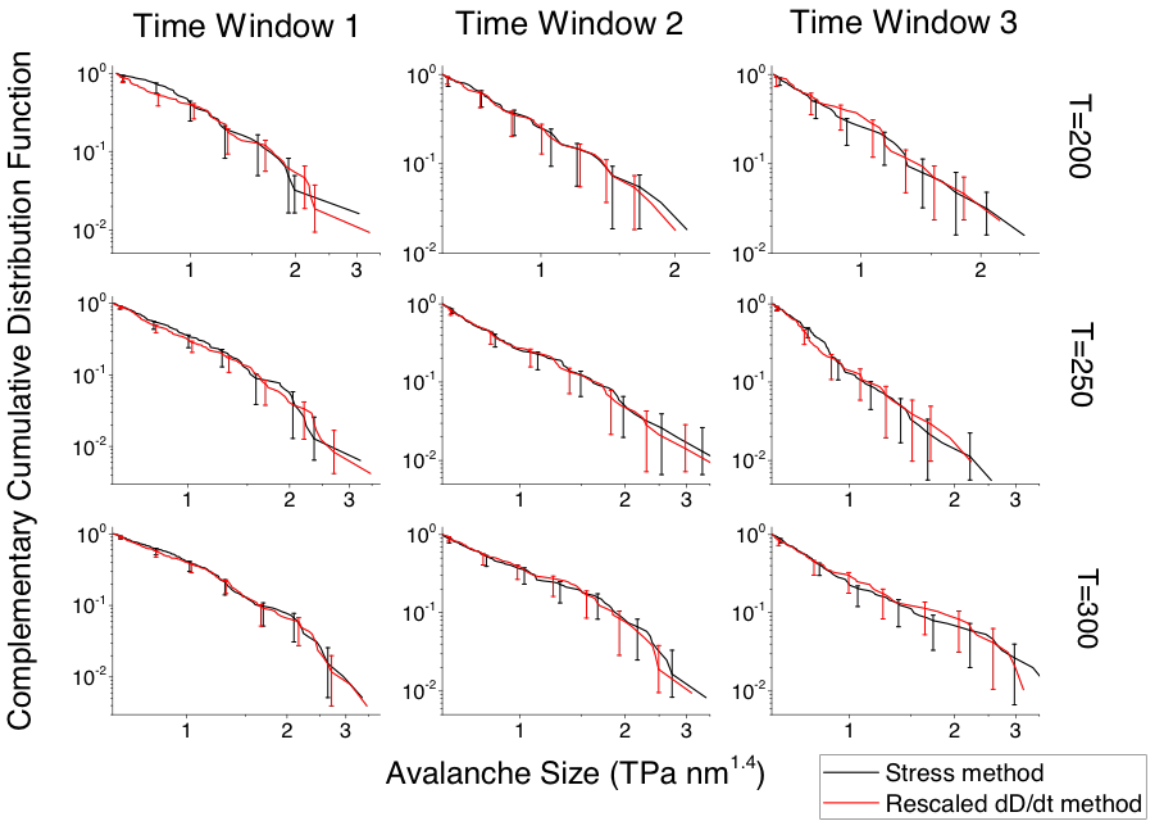

Fig. 13: CCDFs of the slip avalanche size taken from indentations for three different annealing temperatures. The data is also separated according to when during the trial the avalanche occurred. The time windows correspond to those defined for Fig. 12. Each graph shows two CCDFs: one in which the slip avalanche size is calculated using the first method and the other in which the slip avalanche size is calculated using the second method. To compare the methods directly, the x-axis in the second method was rescaled so that both CCDFs started at the same size. Hence the slip avalanche size is given in the units of the first method, TPa $nm^{1.4}$. The CCDFs appear to be similar in all nine plots, suggesting that the two different methods for detecting and measuring avalanches give similar results.

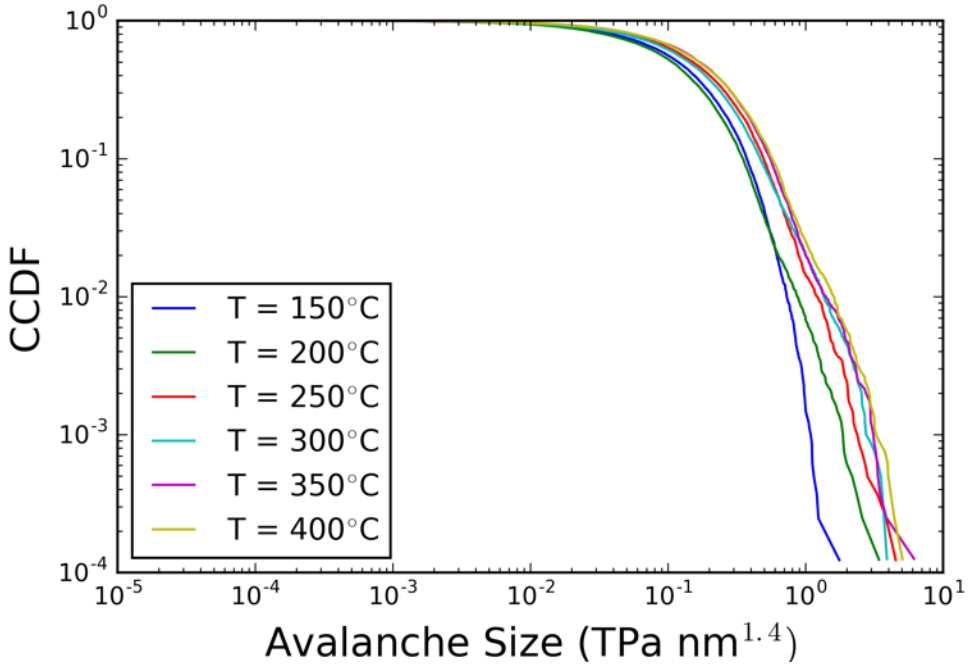

Fig. 14: CCDF of slip avalanche sizes as defined by method 1 without eliminating the smallest detections.

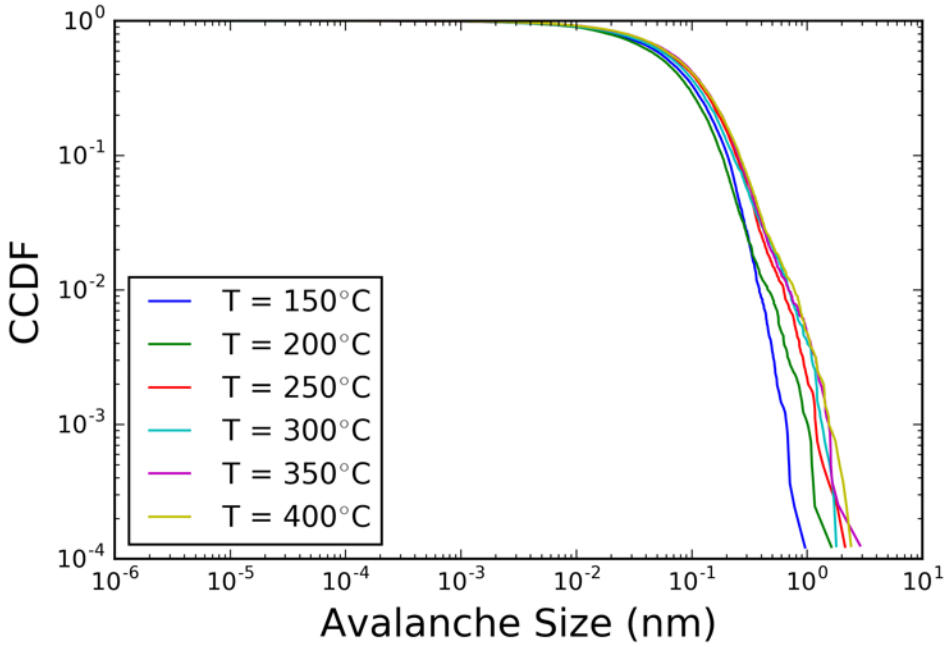

Fig. 15: CCDF of slip avalanche sizes as defined by method 2 without eliminating the smallest detections.

References:

[1] C. A. Schuh, T. C. Hufnagel, and U. Ramamurty, Acta Materialia 55, 12 (2007).

[2] A. Peker and W. L. Johnson, Applied Physics Letters 63, 2342 (1993).

[3] A. Inoue, T. Zhang, and T. Masumoto, Materials Transactions, JIM 31, 177 (1990).

[4] A. L. Greer, Science 267, 1947 (1995).

[5] L. Y. Chen, Z. D. Fu, G. Q. Zhang, X. P. Hao, Q. K. Jiang, X. D. Wang, Q. P. Cao, H. Franz, Y. G. Liu, H. S. Xie, S. L. Zhang, B. Y. Wang, Y. W. Zeng, and J. Z. Jiang, Phys. Rev. Lett. 100, 075501 (2008).

[6] C. A. Schuh and T. G. Nieh, Acta Materialia, 51, 1, (2003).

[7] J. Antonaglia, W. J. Wright, X. Gu, R. R. Byer, T. C. Hufnagel, M. LeBlanc, J. T. Uhl, and K. A. Dahmen, Phys. Rev. Lett. 112, 155501 (2014).

[8] J. Antonaglia, X. Xie, G. Schwarz, M. Wraith, J. Qiao, Y. Zhang, P. K. Liaw, J. T. Uhl, and K. A. Dahmen, Scientific Reports 4, 4382 (2014).

[9] D. C. Hofmann, J. Suh, A. Wiest, G. Duan, M. L. Lind, M. D. Demetriou, and W. L. Johnson, Nature, 451, 7182, 1085 (2008).

[10] Y. H. Liu, G. Wang, R. J. Wang, D. Q. Zhao, M. X. Pan, and W. H. Wang, Science 315, 5817, 1385 (2007).

[11] J. J. Kim, Y. Choi, S. Suresh, and A. S. Argon, Science 295, 5555, 654 (2002).

[12] Y. Li, Q. Guo, J. A. Kalb, and C. V. Thompson, Science 322, 5909, 1816 (2008).

[13] W. L. Johnson, G. Kaltenboeck, M. D. Demetriou, J. P. Schramm, X. Liu, K. Samwer, C. P. Kim, and D. C. Hofmann, Science 332, 6031, 828 (2011).

[14] J. J. Lewandowski and A. L. Greer, Nature Materials 5, 1, 15 (2006).

[15] C. A. Schuh and A. C. Lund Nature Materials 2, 7, 449 (2003).

[16] D. Jang and J. R. Greer, Nature Materials, 9(3), 215 (2010).

[17] S. Ding, Y. Liu, Y. Li, Z. Liu, S. Sohn, F. J. Walker, and J. Schroers, Nature Materials, 13(5), 494 (2014).

[18] M. D. Demetriou, M. E. Launey, G. Garrett, J. P. Schramm, D. C. Hofmann, W. L. Johnson, and R. O. Ritchie, Nature Materials 10(2), 123 (2011).

[19] L. Tian, Y. Cheng, Z. Shan, J. Li, C. Wang, X. Han, J. Sun, and E. Ma, Nature Communications 3, 609 (2012).

[20] K. J. Laws, D. B. Miracle, and M. Ferry, Nature Communications 6, 8123 (2015).

[21] F. Meng, K. Tsuchiya, S. II, and Y. Yokoyama, Applied Physics Letters 101, 121914 (2012).

[22] A. Slipenyuk and J. Eckert, Scripta Mater 50 (2004).

[23] G. Kumar, P. Neibecker, Y. H. Liu, and J. Schroers, Nature communications 4, 1536 (2013).

[24] H. Huang, J. Zhang, C.-H. Shek, and J. Yan. Journal of Alloys and Compounds, 674,223–228, (2016).

[25] K. A. Dahmen, Y. Ben-Zion, and J. T. Uhl, Phys. Rev. Lett. 102, 175501 (2009).

[26] A. C. Fischer-Cripps, Nanoindentation, Mechanical Engineering Series (Springer, 2002).

[27] Wendelin J. Wright, Yun Liu, Xiaojun Gu, Katherine D. Van Ness, Steven L. Robare, Xin Liu, James Antonaglia,Michael LeBlanc, Jonathan T. Uhl, Todd C. Hufnagel, and Karin A. Dahmen, Journal of Applied Physics 119, 084908 (2016); doi: 10.1063/1.4942004.

[28] D. S. Fisher, K. A. Dahmen, S. Ramanathan, and Y. Ben-Zion, Phys. Rev. Lett. 78, 4885-4888 (1997).

[29] J. Lin, E. Learner, A. Rosso and M. Wyart, PNAS 111, 14382–14387 (2014).

[30] K.M. Salerno, C.E. Maloney, M.O. Robbins, Phys. Rev. Lett. 109, 105703 (2012).

[31] K. A. Dahmen, Y. Ben-Zion, and J. T. Uhl, Nat Phys 7, 554 (2011).

[32] J. P. Sethna, K. A. Dahmen, and C. R. Myers. Crackling noise.Nature 410, 242-250 (2001).